PERGAMON

International Journal of Heat and Mass Transfer 41 (1998) 2991–3004

International Journal of HEAT and MASS TRANSFER

Application of a photographic method for determining mass transfer to flow around a submerged parallelepiped

Paul M. Schlosser,[a]* Matthew N. Godo,[a]† Timothy D. Fornes,[b] Elaine Cohen Hubal[b]‡

[a]*Chemical Industry Institute of Toxicology, P.O. Box 12137, Research Triangle Park, NC 27709-2137, U.S.A.*
[b]*Department of Chemical Engineering, North Carolina State University, Raleigh, NC 27695-7905, U.S.A.*

Received 20 December 1996; in final form 5 December 1997

Abstract

A previously described method for quantifying uptake of dilute photographic developer solutions (Dasgupta et al., Int J Heat Mass Transfer 1995;38:2029–37) [1] was applied to the floor of a recirculating flow tank near a submerged parallelepiped. The method was calibrated for a new combination of film and developer. Unlike [1], we found it preferable to include an autocatalytic term in the rate equation for silver development to adequately describe the kinetics of development. A map of mass transfer resistance between the bulk fluid and the flow tank floor was generated for future comparison to CFD predictions.

Nomenclature

CFD computational fluid dynamics
C_H, C_{H0}, C_{Hs} concentrations of hydroquinone in the film emulsion, diluted developer, and stock developer [kmol m^{-3}]
C_{S0}, C_S concentration of silver in the film, initially (latent image) and at a later time [kmol m^{-3}]
C_{SB0}, C_{SB} concentration of silver bromide in the film, initially and at a later time [kmol m^{-3}]
D_H effective diffusivity of hydroquinone in developer solution (water) [m^2 s^{-1}]
h mass transfer coefficient between the film surface and the bulk developer solution [m s^{-1}]
k_1, k_2 rate constants for the autocatalytic model [m^6 kmol^{-2} min^{-1}] and the noncatalytic model [m^3 kmol^{-1} min^{-1}]
k_r', k_r lumped parameter rate constants for the autocatalytic and noncatalytic models [min^{-1} %$^{-1}$]
L thickness of film emulsion [m]
m variable auto-catalytic power
n stoichiometric proportionality between hydroquinone consumption and silver reduction
OD, OD_0, OD_∞ optical density of fully exposed film that has been partially developed, processed with 0% developer, and fully developed
OD′ normalized optical density
PPD parallelepiped
r_H, r_{SB} rate of depletion of hydroquinone and silver bromide [kmol m^{-3} s^{-1}]
SD spinning disk
t time [min]
X developer dilution from concentrated stock [%]
Xt dilution · time product [min · %]

Greek symbols
α optical extinction coefficient [m^2 kmol^{-1}]
β' lumped calibration parameter [m s^{-1}]
λ equilibrium hydroquinone concentration ratio between dilute developer (water) and the film emulsion
ν kinematic viscosity [m^2 s^{-1}]
ω rotational speed [rad s^{-1}].

* Corresponding author. Tel.: 001 919 558 1243; fax: 001 919 558 1300; e-mail: schlosser@ciit.org.
† Current address: Fluid Dynamics International, Inc., Rose Tree Corporate Center II, Suite 1060, 1400 N. Providence Road, Media, PA 19063, U.S.A.
‡ Current address: U.S. EPA, National Exposure Research Laboratory, HEAB (MD-76), Research Triangle Park, NC 27711, U.S.A.

0017–9310/98 $19.00
PII: S0017-9310(98)00013-1

1. Introduction

Airflow plays an important role in regional upper respiratory tract (URT) dosimetry and interspecies differences in response to inhaled gases and vapors. For example, differences in inspiratory flow fields resulting from differences in airway geometry may account for differences in distribution and severity of formaldehyde-induced URT lesions in rhesus monkeys as compared with rats [2, 3]. Gaining an understanding of the influence of airflow upon exposure of humans and animals to potentially harmful materials through the use of computational fluid dynamics (CFD) (e.g., [4]) is theoretically possible. This approach involves two steps. First, numerical simulations, refined by comparison to experimental studies, are performed to establish the characteristics of airflow for a given nasal geometry. Next, local uptake patterns are obtained by combining the airflow results with mass balance equations for a dilute, diffusing chemical species and appropriate mass transfer boundary conditions at the airway surface.

The one drawback to this approach is that directly validating CFD predictions of localized gas uptake is difficult due to the scale and geometry of nasal structures and the biochemical processes that occur subsequent to gas uptake. Given uncertainties about the accuracy of the CFD methods in these complex geometries and the appropriate boundary conditions for a given chemical, some means of testing CFD methods is desired before they can be confidently used to predict gas uptake, and hence risk from exposure, in humans.

The purpose of this study was to measure local uptake of a dilute chemical from a fluid flow field that is similar in complexity to those occurring in the URT for comparison to mass flux predictions obtained via CFD. We quantified mass transport to the floor of a large recirculating flow tank in the region of a submerged parallelepiped (PPD). The submerged PPD was selected on the basis of several criteria. First, its geometry is easy to reproduce with a computational grid and hence the description of complex geometry as a confounding factor is eliminated. Second, despite this geometric simplicity, complex flow patterns are produced that can be used to assess the predictive abilities and limitations of CFD software. Third, the geometry does bear a crude similarity to the middle turbinate in primates. Finally, by working in this aqueous system, we can apply an existing method for experimentally measuring mass transfer resistance to the flow tank floor [1].

Flow around submerged objects has been well documented in the literature. In a review by Lugt [5], the presence of a horseshoe or necklace vortex in the flow around an obstruction has been illustrated. A closer examination of this phenomenon revealed that flow around a cylinder produces either a 2-, 4-, or 6-vortex system, depending on the Reynolds number [6]. Using a variety of experimental and theoretical techniques, Hunt et al. [7] were able to simultaneously describe the many vortex systems associated with flow around a cube and the difficulties in providing a simple illustration of the location and size of these flow features for a three-dimensional geometry (see Fig. 1). Numerical simulations of the horseshoe vortices remain limited. Recently, Deng and Piquet [8] presented a numerical technique that could

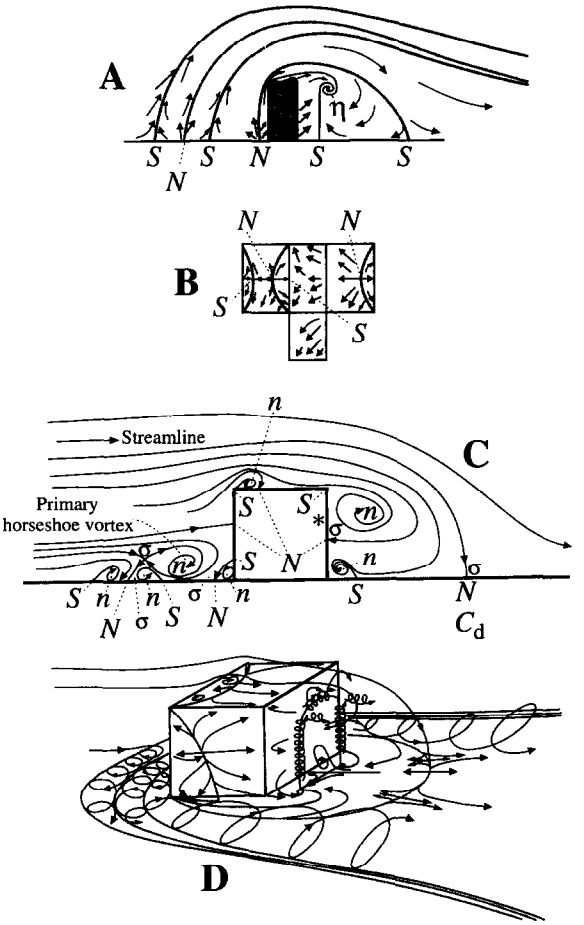

Fig. 1. Mean streamlines, singular points and flow pattern around a cuboid and a cube. (A) On the centre-line of a cuboid: plan view of shear-stress on the surface. (B) Shear-stress lines on the top and sides of the cube. (C) On the centre-line of a cube. (D) Sketch of the flow pattern around the cube. N, node of attachment of streamline pattern to a surface; S, surface saddles of streamline pattern; n, node of streamline pattern interior to flow; η, interior node of separation; σ, saddle of streamline pattern interior to flow; $*$ centre-line separation point at rear of obstacle; C_d, downstream centre-line zero-stress point. (Adapted from J. C. R. Hunt, et al. Kinematic studies of the flows around free or surface mounted obstacles; applying topology to flow visualization. J Fluid Mech 1978;86:179–200. Copyright 1978 by Cambridge University Press. Reprinted with permission of Cambridge University Press.)

be used to examine incompressible, three-dimensional turbulent viscous flow about an aerofoil-flat plate junction. They concluded that the main features of the horseshoe vortex were correctly captured. These features include the location of the primary vortex center, the size of the secondary root vortex, and the existence of a small trailing edge root separation. They did note, however, the thin foil boundary layer was not captured due to a lack of resolution in the transverse horizontal direction.

Studies of mass (or heat) transfer for flow around submerged objects are limited, particularly for objects resting on a surface. Goldstein et al. [9] used naphthalene sublimation to measure the local enhancement of transport in the vicinity of cylinders with varying height-to-diameter ratios. They were able to illustrate the presence of several local maxima in transport rates that were located immediately upstream and downstream from the cylinder as well as on either side of the cylinder. Using a liquid crystal sheet, Ichimiya et al. [10] examined heat transfer for flow around a cylinder for a range of cylinder dimensions and flow rates. Their general conclusions were in agreement with Goldstein et al. [9]. They also noted that the downstream local maximum in heat transfer rates, resulting from augmentation by the presence of the horseshoe vortex, was confined to a distance range of one to three times the cylinder diameter. To date, there has been no specific effort to predict mass transfer patterns that result from flow around a submerged parallelepiped, perhaps because of limited practical interest. Dasgupta et al. [11] examined this system experimentally and observed a fairly complex, and beautiful, mass transfer pattern. Given the difficulties associated with correct reproduction of the horseshoe vortex phenomena by numerical techniques, it is not surprising that no numerical studies of mass transfer have been performed. The problem is particularly challenging since surface mass transfer occurs where mass and momentum transport gradients are greatest and resolution is most difficult to obtain.

For flow around a submerged PPD, the experimental results of Dasgupta et al. [11] identified several robust features of the mass transfer pattern. These patterns are illustrated by the developed images from completely exposed pieces of photographic film placed on the flow-tank floor and subject to the flow of a dilute developer solution. (Figure 2 shows an example of such an image from our own laboratory; see Methods section for details.) Local uptake enhancement was seen to occur in three well-defined areas: a horseshoe-shaped region, a peripheral fringe surrounding the horseshoe, and a downstream medial wake. Local uptake depletion occurred immediately aft of the PPD and in shoulder regions further downstream.

We applied the method of Dasgupta et al. [1] to experimentally quantify mass transfer resistance between the bulk fluid and the flow-tank floor. Dasgupta et al. proposed two possible models for the kinetics of film development, one without and one with an autocatalytic term for silver development. Models for the two cases fit the calibration data almost equally well, and the noncatalytic model was selected since its numerical goodness of fit was the better of the two and because the estimated value of a parameter in the autocatalytic model was unrealistically small. The results from our calibration experiments, for a different combination of film and developer than that used by Dasgupta et al., indicate that the autocatalytic model is superior. Using the calibration parameters for the autocatalytic model, the equation was then applied to data from a set of flow tank experiments, and a map of mass transfer coefficients on the flow tank floor near the PPD was generated. These experimentally determined coefficients will be compared to those predicted using CFD in a subsequent paper.

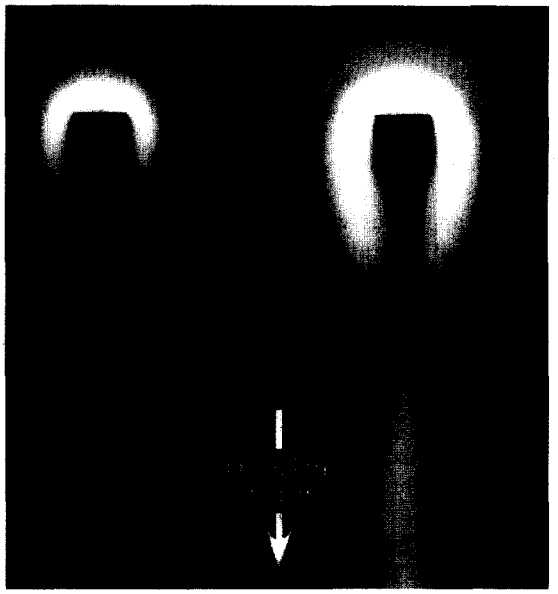

Fig. 2. Developed images from flow tank floor with two parallelepipeds. The observed optical patterns are the result of variations in mass transfer resistance that, in turn, result from the flow field induced by the parallelepipeds.

2. Experimental methods

The general approach employed a spinning disk (SD) apparatus, for which mass transfer coefficients are known from theory, to parameterize and calibrate a mathematical model of film development as a function of mass transfer resistance in the developer solution. Film was placed on the floor of a recirculating flow tank with a parallelepiped (PPD) positioned on top of the film, and was subjected to the flow of dilute developer for known

lengths of time. The rate of optical development at specific locations on the flow-tank floor was then measured and mass transfer resistance at those locations quantified using the calibration equation.

2.1. Spinning disk experiments

A SD apparatus was used to provide data for the selection and calibration of a model relating mass transfer and film development. SD experiments were similar to those described in Dasgupta et al. [11]. Photographic film (Kodak Technical Pan Film, TP4415, 8 × 10 in, Estar Thick Base) was cut into 5.5 cm diameter disks. The disks were placed 15 cm directly below a 100 W incandescent bulb for 20 min. The film was then dipped in water and placed on the underside of a 6.3 cm diameter Teflon disk-spindle with a threaded steel inner shaft that was attached to a RPM rotator (Model ASR2, Pine Instrument Company). The shape of the Teflon disk-spindle, shown in Fig. 3, differed from that used by Dasgupta et al. The spindle was constructed to provide maximum overall mass transport as well as optimum fluid flow [12]. The disk was then lowered into a 4-L, clear vessel (14.5 cm wide) that contained dilute Kodak HC-110 film developer and rotated approximately 8 cm below the liquid surface at a given speed for a given length of time.

Experiments were performed at rotational speeds of 40, 80, 120, 160, and 200 rpm; development times of 2–32 min; and developer dilutions of 0.2, 0.4, and 0.8%. For each individual run, a fresh batch of dilute developer was used. Rotational speeds ranged from the lowest obtainable on the apparatus to the speed at which mass transfer resistance in the liquid phase is negligible (when maximum optical density (OD) occurs for a given dilution and development time). Developmental times were chosen such that highest OD levels would be approximately four. Developer dilutions were chosen to span the dilutions used in the flow tank (≈0.38%).

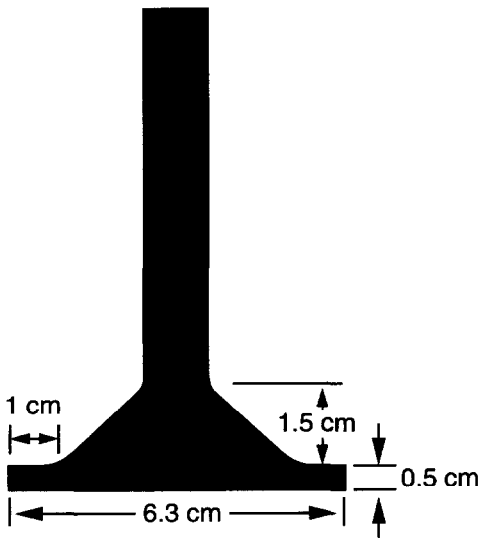

Fig. 3. Schematic of spinning disk spindle.

At the end of each experiment, the film was removed from the apparatus and placed in Kodak Stop Bath for 30 s. The film was then fixed for 5 min using Kodak fixer, cleared using Kodak Hypo Clearing Agent, and finally rinsed for 15–20 min. Three regions from each film disk were scanned with an optical densitometer (see below). The individual OD values from all three regions were averaged to give a single OD value for each film disk.

In addition to the measurements described above, values for OD_0, OD at dilution · time = 0% · min, and OD_∞, the maximum OD achievable, were needed. OD_0 was determined using the SD procedure described above with a 0% developer solution. Three trials were performed at the minimum and maximum rotational speeds for 2 min and OD_0 set to the average for all six trials.

Direct measurement of OD_∞, in which pieces of film were developed overnight, processed and scanned as for OD_0, gave high OD values that varied widely over the surface of the film, with many at (or above) the densitometer's limit of 10. Optical density is the logarithm of the ratio of the incident light intensity to the transmitted light intensity: OD = ln(incident/transmitted). So as the transmitted intensity diminishes, and OD increases, the accuracy with which OD can be measured diminishes. The scanning densitometer used in these experiments had suggested range of 0–4 (transmitted light between 100 and 1.8% of incident). Hence, the accuracy of OD readings much greater than four is suspect, which was the case for the film developed overnight, so we decided that the measured values were too inaccurate to use. Instead OD_∞ was treated as an adjustable parameter in fitting the model to the spinning disk data (below). It was also decided that OD data from the flow tank which clearly exceeded a value of four would not be used (i.e., if all three values in the triplicate were greater than 4.0).

2.2. Flow-tank apparatus

A recirculating flow tank of rectangular cross section (20 × 16.8 cm), which has been described elsewhere [11], was used. For this work, several modifications were made (see Fig. 4(a)). First, two additional four-blade propellers (10 cm diameter) were added to the original four-blade propeller configuration to increase the flow rate and improve mixing. Vibrations within the flow tank were reduced by mounting the drive motor (1/3 hp, Reliance DC-1, Reliance Electric Co., Cleveland, OH) on an aluminum shaft (2.54 cm diameter) and placing the flow tank on a vibration isolation support system consisting of 1 in box iron, dense cell Styrofoam (1/2 in thickness) and neoprene rubber (1/8 in thickness). To align the flow and dampen secondary flow patterns that occurred in

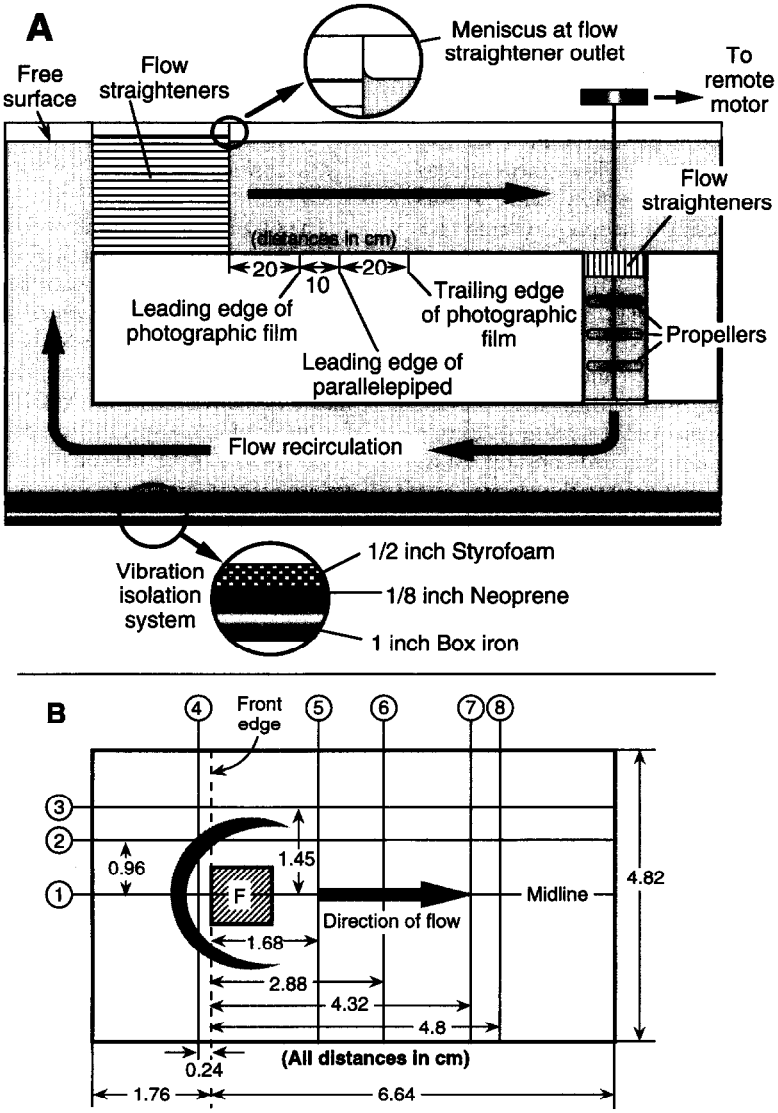

Fig. 4. (A) Schematic of flow tank apparatus. (B) Schematic of flow tank floor and photographic film region analyzed for mass transfer. F is the footprint of the parallelepiped. The actual film area extended well beyond the area indicated here. To compare mass transfer coefficient (h) values obtained in this study with predictions from computational fluid dynamics, values of h were plotted as a function of position along each of the cross sections identified by a number in the circle at one end of the section.

the open channel, two mufflers constructed using plastic drinking straws were added, one at the inlet to the test section and the other immediately inside the cylindrical duct that housed the three propellers.

The inlet velocity was measured by following the motion of a 1% aqueous solution of basic fuchsin (Aldrich Chemical Co., Milwaukee, WI) introduced into the flow field using a syringe pump (Model 355, Orion Research Inc., Cambridge, MA), with the syringe (10 cc) connected to a fine, long needle (28G 2, ID 0.006 in), via a short length of polyethylene tubing followed by a 30 cm piece of stainless steel tubing (1/16 in ID), which was subsequently secured in place using a micro-manipulator (Leitz, Germany). Dye streak fronts were created by perturbing the dye stream and their motion was recorded using a video camera (CCD72, MTI Dage, Michigan City, IN) connected to a video recorded (AG 6300, Panasonic, Secaucus, NY). Real time information was added to the video tape using a time-date generator (WJ-810, Panasonic). The distance traveled by the dye streak was measuring using plastic laminated grid (0.1 cm divisions) mounted on the floor and back wall of the flow tank.

Axial fluid speed was determined from frame-by-frame analysis of the video tapes, with five separate measurements at a number of points in the flow field near the inlet.

One flow rate was studied, with a maximum velocity of 2.94 cm s^{-1} in the direction of flow (measured as described above at the core of the flow field). It was reproducibly obtained by using a neoprene O-ring (1/8 in diameter) to connect the propeller drive shaft to a stainless steel pulley mounted directly to the electric motor. The motor speed, controlled using a DC controller (DC1-70G, Reliance Electric Co., Cleveland, OH), was operated at the lowest setting to minimize vibrations and the stainless steel pulley was burnished to prevent slippage. The flow rate was checked several times during the course of the studies, and remained constant. Mass transfer studies were performed around the vicinity of a stainless steel PPD (grade 316; $1 \times 1 \times 4$ cm; dimensions to within 0.0025 cm), constructed by the Maintenance Department, Chemical Industry Institute of Toxicology. The location and size of the photographic/mass transfer features was sensitive to flow rate, so constancy of flow rate will be confirmed by the extent that these are reproducibly created.

2.3. Mass transfer measurements

To obtain mass transfer patterns near the PPD, the following approach was used. A black background laminated in plastic was placed on the floor of the flow tank. The laminate was kept in place by a thin layer of high-vacuum grease. The tank was filled with water (105.3 L) and allowed to come to room temperature overnight. A volume of 0.4 L of photographic developer solution (Kodak HC-110, Eastman Kodak Co., Rochester, NY) was added to the tank 1 h prior to any experiments to allow for complete mixing. Before the film was placed in the flow tank, it was exposed to a 60-Hz fluorescent light fixture at a distance of 6 feet for 15 min on the day of the experiment. (In both these and the calibration experiments, the exposure was presumed to be essentially complete.) Following this pre-exposure, films were replaced in their original packaging until use. A single sheet of photographic film (Kodak Technical Pan Film, TP4415, 8×10 in, Estar Thick Base) was placed on the bottom of the upper portion of the flow tank (Fig. 4(A)) and centered with respect to the 20-cm width of the flow tank. After positioning the film, the PPD was placed on top and in the center of the film, 10 cm from the leading edge of the film. Consistent placement of the PPD was accomplished using a plastic insert. A series of film developer contact times (2, 4, 8, 16, 32 and 64 min) was examined. The start of an experiment was the moment at which the PPD was properly positioned on the film.

After removal from the flow tank, the photographic film was rinsed using Kodak Indicator Stop Bath for 30 s, fixed in Kodak Rapid Fixer for 4 min and washed in water for 60 min. All photographic chemicals and wash water were maintained at room temperature.

2.4. Densitometry

The OD of the flow tank and SD photographic negatives was quantified with a scanning densitometer (LKB Ultroscan XL Enhanced Laser Densitometer, Bromma, Sweden). Scans were performed remotely on a personal computer using a Gelscan XL software package (Pharmacia AB, Bromma, Sweden). The resulting Gelscan XL files were converted to an ASCII format that is suitable for importing to a spreadsheet program.

Each Gelscan XL file contained a single column of OD values, corresponding to a set of a discrete location on the film with x, y-coordinates, x_i, y_j, $i = 1, \ldots, N$, $j = 1, \ldots, M$. But the actual coordinates were not recorded. Therefore, each file from a flow-tank experiment was parsed into a grid of rows and columns based on the location of the PPD footprint, which was evident as sets of low ODs obtained as the scanner repeatedly moved over that region of film. (The number of entries in each column was determined by the frequency at which the scanner passed over the footprint.) After this conversion, the grid was cropped to a specific number of rows and columns relative to the location of the footprint, as indicated in Fig. 4(B). The OD values from a given row and column (e.g., row 3, column 20) in the set of grid files for all development times and experimental repetitions were then assumed to all have the same x–y location, and so yielded a time course of OD at that location in triplicate. To test this assumption and the reproducibility of the procedure (including film exposure and development), plots of OD as a function of row or column position for each scanned image, were compared. Reproducible of these plots (at a given development time) and the extent to which primary features such as local OD minima and maxima were aligned for all scanned images were used to validate this assumption and overall reproducibility (including flow rate).

Finally, to obtain the distance between subsequent x and y values, a rectangle 5×9 cm was drawn on a blank piece of paper, scanned by the densitometer, parsed in the same way as a flow-tank image, and the number of rows and columns within the rectangle were counted.

3. Mathematical modeling

The models for film development and the subsequent calibration equations were developed by Dasgupta et al. [1]. We describe the models here briefly.

3.1. Film development calibration equation

The film emulsion was treated as a homogeneous volume of thickness L in which silver bromide is reduced to metallic silver by a developing agent that was presumed to be hydroquinone (see comment below). Two possible rate equations were considered for the development process,

$$r_{SB} = k_1 C_H C_{SB} C_S \tag{1a}$$

and

$$r_{SB} = k_2 C_H C_{SB} \tag{1b}$$

where r_{SB} is the rate of silver bromide reduction, k_1 and k_2 are rate constants, and C_H, C_{SB}, and C_S are the concentrations of hydroquinone, silver bromide, and silver in the emulsion, respectively. Equation (1a) presumes that the process is autocatalytic (i.e., the rate accelerates with increasing concentration of the product, C_S), while (1b) does not. Below, we refer to the case using (1a) as the autocatalytic model and the case using (1b) as the noncatalytic model. In either case, the rate of change of C_{SB} in the emulsion is given by

$$\frac{dC_{SB}}{dt} = -r_{SB}. \tag{2}$$

A mass balance on silver atoms in the emulsion allows one to solve for C_S as a function of C_{SB},

$$C_S = (C_{SB0} + C_{S0}) - C_{SB} \tag{3}$$

for either model, where C_{SB0} and C_{S0} are the initial concentrations of silver bromide and silver in the emulsion, respectively. (Exposure to light converts some silver bromide to silver, creating a latent image, and hence $C_{S0} > 0$.)

When mass transfer resistance between the film and the bulk fluid is negligible the concentration of H in the bulk fluid, C_{H0}, is assumed to be at equilibrium with C_H:

$$C_{H0} = \lambda \cdot C_H \tag{4}$$

where λ is the equilibrium constant. Since the concentration of H in the developer was not known (proprietary information), a dilution factor, X, was defined to be the ratio of H in the bulk fluid, C_{H0}, to that in undiluted developer, C_{Hs}:

$$X \equiv C_{H0}/C_{Hs}. \tag{5}$$

OD was presumed to obey the Beer–Lambert law of light transmission as a function of C_S:

$$OD = OD_0 + (\alpha L)(C_S - C_{S0}) \tag{6}$$

where OD_0 is the OD of undeveloped film. Maximal optical density, OD_∞, was identified with complete conversion of silver bromide to silver. Making use of this identity, along with (3) and (6), yielded:

$$OD = OD_0 + (OD_\infty - OD_0)(1 - C_{SB}/C_{SB0}). \tag{7}$$

OD_0 was set to the OD of film from the SD experiments run at 0% developer concentration.

Using (4) and (5) to substitute for C_H in (1a) or (1b), and (3) to substitute for C_S in (1a), equation (2) was solved for C_{SB}. Substituting the solutions of (2) into (7) gave:

$$OD = OD_0 + (OD_\infty - OD_0)\left(\frac{1 - \exp[-k_r' \cdot (Xt)]}{1 + \Phi \cdot \exp[-k_r' \cdot (Xt)]}\right) \tag{8a}$$

for the autocatalytic model and

$$OD = OD_0 + (OD_\infty - OD_0)\{1 - \exp[-k_r \cdot (Xt)]\} \tag{8b}$$

for the noncatalytic model, where $\Phi = C_{SB0}/C_{S0}$, $k_r = k_2 \cdot C_{Hs}/\lambda$, and $k_r' = k_1 \cdot C_{Hs}(C_{SB0} + C_{S0})/\lambda$. At high rotational speeds, mass transfer resistance between the bulk fluid and the film surface in the SD experiments is negligible, so equations (8a) and (8b) could be compared to SD time-course data for OD to select one model for further analysis.

Under conditions where mass transfer resistance is significant, the flux of H to the film surface, r_H, is proportional to the difference between the bulk concentration and the concentration that would be in equilibrium with the emulsion:

$$h \cdot (C_{H0} - \lambda \cdot C_H) = r_H \cdot L \tag{9}$$

where h is the mass transfer coefficient. Assuming a fixed stoichiometry between the flux of H and the rate of development, $n = r_H/r_{SB}$, and making use of the equation for r_{SB} (i.e., (1a) or (1b), depending on which model is being considered) one can solve for C_H in terms of C_{SB}, h, and other system parameters. Dasgupta et al. [1] gave the solution for the noncatalytic model but not for the autocatalytic model. Solving the autocatalytic model yielded:

$$C_H = (C_{H0}/\lambda)[1 + n \cdot L \cdot k_1 \cdot C_{SB} \cdot C_S/(h \cdot \lambda)]. \tag{10}$$

Substituting (10) back into (1a), using the conversion

$$OD' = \frac{OD - OD_0}{OD_\infty - OD_0}$$

and making use of the other substitutions described above for the case with no mass transfer resistance, equation (2) became our autocatalytic calibration equation:

$$\frac{dOD'}{dXt} = \frac{(1 - OD')(\Phi \cdot OD' + 1)k_r'}{\Phi + 1 + (\beta'/h)(1 - OD')(\Phi \cdot OD' + 1)} \tag{11}$$

where

$$\beta' = n \cdot L \cdot C_{SB0} \cdot k_r'/C_{Hs}.$$

Dasgupta et al. [1] obtained a similar differential equation for C_{SB} from the noncatalytic model, which they solved analytically. Equation (11) was solved to obtain

$$F(OD', h) = [\ln(1 + \Phi \cdot OD') - \ln(1 - OD') + (\beta' \cdot OD'/h)]/k_r' = Xt \tag{12}$$

but an analytical inverse, giving OD′ as a unique function of Xt, cannot be obtained.

Since X and t were the independent variables in these experiments, fitting (12) to our data was presumed not

to be statistically appropriate (rigorous). Therefore we used SimuSolv Modeling and Simulation Software (Dow Chemical Company, Midland, MI) to numerically integrate (11), after which the absolute OD was calculated from OD′ using the values of OD_∞ (selected as an adjustable parameter) and OD_0 (measured). The resultant OD predictions were compared to measured OD values at specific values of X and t, with goodness of fit quantified by SimuSolv's log-likelihood function.

For a spinning, flat disk, the mass transfer-coefficient, h, is a constant across the disk surface, given by:

$$h = 0.621 \cdot D_H^{2/3} \cdot \nu^{-1/6} \cdot \omega^{1/2} \tag{13}$$

where ω is the rotation speed of the disk in rad s^{-1}, ν is the viscosity of dilute developer, taken to be 10^{-6} m^2 s^{-1}, and D_H is the diffusivity of H [13]. D_H, was estimated by Dasgupta et al. [1] using the Wilke–Chang equation to be $8.3 \cdot 10^{-10}$ m^2 s^{-1}. Using this value in (13), and substituting the result into (11), the remaining unknown parameters are Φ, β', OD_∞, and k_r'. Values for these parameters were estimated using the SimuSolv optimization routine to fit (11) to SD data.

3.2. Application of flow-tank data

While fitting the differential calibration equation (11) using the SimuSolv optimization routine to a relatively small set of time-course data sets was possible, it was not feasible to do so for the very large sets generated from the flow-tank experiments. A FORTRAN program was created to fit equation (12) to large sets of time-course data in an automated manner by a least-squares method. In particular, for pairs (OD_i, Xt_i), $i = 1, \ldots, n$, the sum of square errors (SSE) given by:

$$SSE = \sum_{i=1}^{n} [F(OD_i, h) - Xt_i]^2$$

was minimized with respect to h [F given by equation (12)]. The minimum was determined as the value of h for which $dSSE/dh = 0$:

$$h_{SSE} = \frac{\beta' \cdot \sum_{i=1}^{n} (OD_i')^2}{\sum_{i=1}^{n} OD_i' \cdot [\ln(1 - OD_i') - \ln(1 + \Phi \cdot OD_i') + k_r' \cdot Xt_i]}.$$

Since the value of h so obtained was not necessarily the most likely statistical value, values of h obtained by this method were compared to those obtained using SimuSolv to fit equation (11) for representative time-course data sets, spanning the range of mass transfer rates observed, to assure that the two methods yielded similar results.

4. Results

The Kodak TP4415 black and white pan film performed quite well in the flow-tank experiments. A representative image is shown in Fig. 2. The images contain a fine level of detail, indicating good resolution of local mass transfer patterns.

To check the reproducibility of the flow-tank experiments and our assignment of OD readings to specific locations on the flow-tank floor, OD readings as a function of location and development time were plotted in Fig. 5 along several of the cross-section lines indicated in Fig. 4(B). The region of line 1 where OD dropped to below 0.4 was the footprint of the cube. Overall reproducibility appeared to be quite good. Some regions downstream of the cube (line 7 and right side of line 3) showed higher variability. Visual inspection of the flow in these regions, enhanced by dye streaks, revealed vortex shedding, indicating unstable flow. This behavior was extremely sensitive to the placement of the cube, so lower reproducibility is not surprising. Therefore, these results confirmed our procedure for assigning OD values to specific locations on the film surface relative to the position of the cube. Given that the size and location of all the features were sensitive to the flow-rate, this also indicates that the flow rate was kept reasonably constant.

OD data from the SD experiments were plotted in Fig. 6, where each data point represents the mean $\pm$ s.d. from three disks. The overall mean of the six trials with 0% developer yielded a value of $OD_0 = 0.101 \pm 0.002$. (Since the OD at 0% dilution was independent of rotational speed, it was depicted as the zero dilution · time (Xt) point for the 0.2% data in all plots.) There is a clear delay of about 0.4 min · % before the rate of development accelerates, and the rate appears to drop between the last two Xt values as compared to the previous pair of points, giving the data a sigmoidal shape. The dependence on rotational speed can also be noted.

While the 0.2 and 0.4% dilution data in Fig. 6(A)–(E) are virtually indistinguishable, the 0.8% data appears to differ from some experimental conditions. This indicates that the invariance of OD with respect to the dilution · time product holds for the 0.2 and 0.4% data but may not hold at 0.8%. Therefore we initially combined the 0.2 and 0.4% data into a single set for parameter estimation, keeping the 0.8% data separate. The statistical significance of the difference between the 0.8% data and the remaining data was then considered (see below). Since this difference could only be examined using the calibration equation, it was first necessary to select the equation.

The difference between the 160 and 200 rpm data was negligible. Therefore, the mass transfer resistance between the bulk fluid and the film surface was assumed to be negligible at these higher rotation rates, particularly at 200 rpm. The combined 0.2 and 0.4% dilution data at 200 rpm was then used to compare the two models given by equations (8a) and (8b), respectively. The autocatalytic model performed slightly better than the noncatalytic model, as shown in Fig. 6(F). For the fits shown,

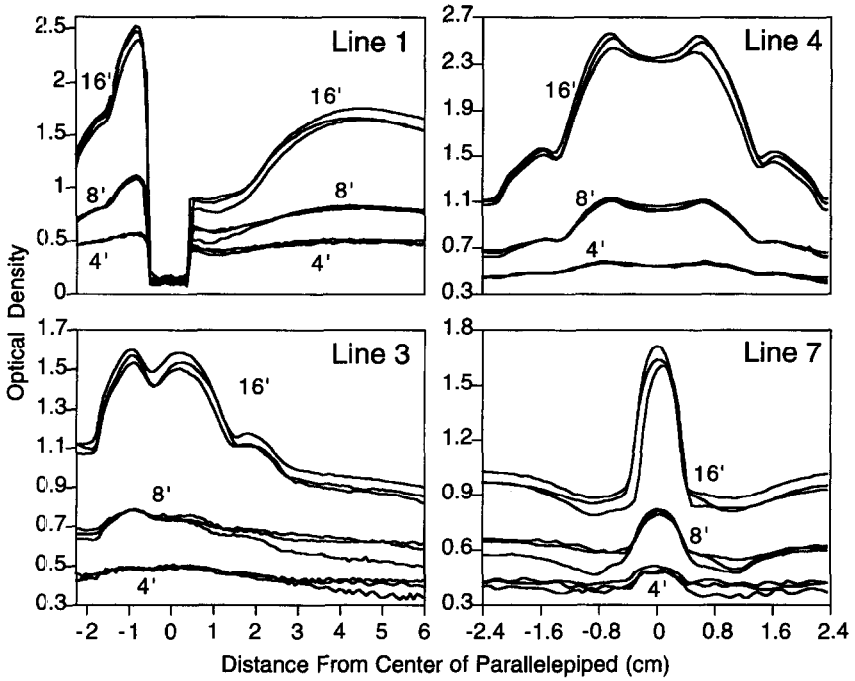

Fig. 5. Optical density measurements along lines specified in Fig. 4(B) for the three images developed at each of three time points (4, 8 and 16 min) demonstrating reproducibility of experimental technique, including flow rate and assignment of individual optical density measurements to specific locations on the film surface.

both models were constrained to match the measured OD at 0% dilution. When this condition was relaxed for the noncatalytic model, the curve did fit all the data except the 0 min·% point quite well (not shown), but this gave a negative value for OD_0. Also, either with or without OD_0 fixed, the noncatalytic model required an OD_∞ on the order of 10^3. Since the autocatalytic model fit better and gave more reasonable parameters values, it was selected as most appropriate.

Visual inspection of the data in Fig. 6 revealed what appeared to be a systematic difference between OD values for the 0.8% dilution data as compared with those for 0.2 and 0.4%, though there were only a few combinations of Xt and rotational speed at which this difference is significant at a 95% confidence level. The most appropriate choice, however, seemed to be between either including or excluding the entire 0.8% data set based on an overall comparison with the 0.2 and 0.4% dilution data. The 0.8% data were compared to the combined 0.2 and 0.4% data by fitting the calibration equation (11) to the two data sets and then comparing the separate parameter estimates. Since the 0.8% dilution data were only collected at $Xt = 1.6$, 3.2, and 6.4 min·%, the 0.2 and 0.4% dilution data was also restricted to these values for this comparison (i.e., data points at 0.4 and 0.8 min·% were not included). The combined 0.2 and 0.4% dilution data yielded a value of $k_r' = 0.67 \pm 0.01$ $(\text{min}\cdot\%)^{-1}$, (mean ± s.e.), while the 0.8% data gave a value of $k_r' = 0.74 \pm 0.03$ $(\text{min}\cdot\%)^{-1}$. Since the value of k_r' for the 0.8% data was outside the 95% confidence interval for the 0.2 and 0.4% dilution data, the 0.8% data was determined to be significantly different from the combined 0.2 and 0.4% dilution data, and so the 0.8% data were excluded when obtaining final parameter estimates for the calibration equation, reported below. Since the dilution in the flow-tank was between 0.2 and 0.4%, use of this data (without the 0.8% data) was expected to yield appropriate parameter estimates.

The calibration equation (11) was fit to the combined 0.2 and 0.4% dilution data, now including values at 0.4 and 0.8 min·%. The parameter values obtained were: $\beta' = (3.1 \pm 0.3) \cdot 10^{-5}$ m s^{-1} (mean ± s.e.), $k_r' = 0.57 \pm 0.04$ $(\text{min}\cdot\%)^{-1}$, $\Phi = 5.6 \pm 0.3$, and $OD_\infty = 5.2 \pm 0.5$. (This value of k_r' differs from 0.67 ± 0.01 $(\text{min}\cdot\%)^{-1}$, obtained in the comparison above, because the data at 0.4 and 0.8% min·% were included for this estimate.) Fits of the model to the experimental data with these parameter values are shown as the solid lines in Fig. 6(A)–(E). Since the fits were good, the model was used with confidence to determine mass transfer coefficients in the flow tank.

Example applications of the differential form of the calibration equation (11) to three representative grid points from the flow tank appear in Fig. 7. The three

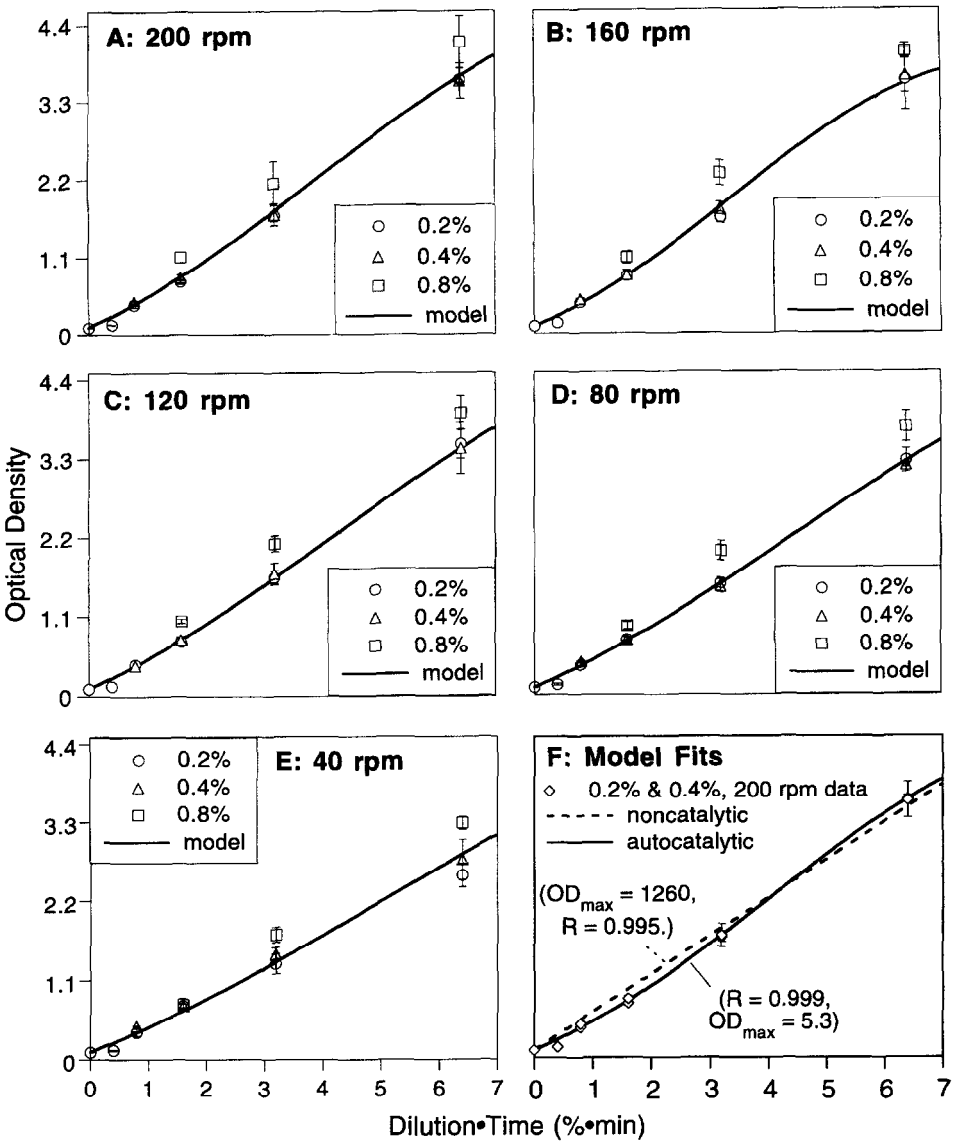

Fig. 6. (A–E) Optical density data from the spinning disk experiments and fit of the autocatalytic model, equation (11), to the combined 0.2 and 0.4% dilution data. (F) Fits of the autocatalytic and noncatalytic models for the case of negligible mass transfer resistance, equations (8a) and (8b), respectively, to the combined 0.2 and 0.4% dilution, 200 rpm data.

points were selected to span the range of observed development rates (mass transfer coefficients). The range of Xt values used in the flow tank did go as high as ~22 min · %, while a maximum of 6.4 min · % was used in the SD experiments, which may explain the lack of fit for the lowest curve in Fig. 7 at short Xt values as compared to longer Xt values. This issue will be addressed in the discussion.

In the region of the flow tank floor selected for analysis (Fig. 4(B)), scanning densitometry gave 8400 grid points. While determining a detailed mass transfer resistance map was not strictly necessary for the purpose of comparison with the CFD software, this would provide a nice representation of the data if it can be done efficiently. The use of the analytic, inverted calibration equation (12) to obtain least-squares estimates of h was compared to values of h obtained with the differential equation form (11) and the log-likelihood objective function of SimuSolv. This comparison was done at a set of 14 grid locations selected to provide a representative span of h values. The results are shown in Table 1. As can be seen in Table 1, the two methods yielded almost identical h

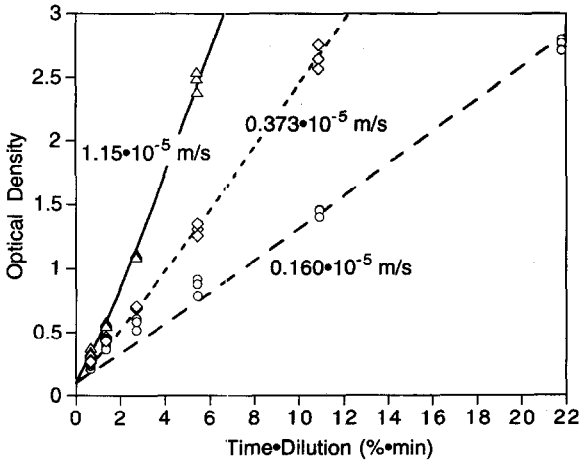

Fig. 7. Example applications of the calibration equation (11) to the time course data from three representative locations on the flow tank floor. The number beside each line is the corresponding mass transfer coefficient.

Table 1
Comparison of estimates for the mass transfer coefficient (h) by two methods

Location	Method	
	Differential[a]	Analytic[b]
1	0.160±0.004	0.162
2	0.190±0.004	0.192
3	0.241±0.004	0.241
4	0.331±0.004	0.331
5	0.373±0.003	0.374
6	0.420±0.006	0.421
7	0.497±0.006	0.498
8	0.555±0.006	0.557
9	0.610±0.005	0.606
10	0.773±0.007	0.788
11	0.82±0.001	0.83
12	0.93±0.01	0.94
13	0.98±0.02	0.99
14	1.15±0.02	1.17

[a] Parameters estimated by use of the differential calibration equation (11), with the log-likelihood objective function in SimuSolv Modeling and Simulation Software. Values are means±s.e.
[b] Parameters estimated by use of the analytic calibration equation (12), with a least-squares objective function. The roles of the independent and dependent variables are reversed during the estimation. Values are point-estimates.

estimates (within one standard error) in all cases but one, and the difference never exceeded 2%. Therefore, the least-squares method was used to obtain a map of h values.

The analytic calibration equation (12) with a least-squares objective function was then applied to the entire data set, 18 images, from the flow-tank experiments. This gave a grid of mass transfer coefficient values corresponding to specific locations on the flow-tank floor. A gray-scale map of the mass transfer coefficients is shown in Fig. 8. While some of the features in this map are not as crisp as they appear in the photographic images (Fig. 2), the primary features are captured. These include the primary and secondary horseshoe-shaped structures that wrap around the cube. Note how the contours fold back on themselves in an elongated S shape along the lower arm of the horseshoe and in an inverted S shape along the upper arm. The other main features are the long tail of higher values extending downstream from the cube and the two comma-shaped areas of lower uptake above and below this tail. More detailed numerical resolution of the mass transfer coefficients along cross-section lines is shown in Fig. 9 (see Fig. 4(B) for locations).

5. Discussion

We applied the general methodology of Dasgupta et al. (1995) to measure mass transfer to the floor of a recirculating flow tank in the vicinity of a submerged parallelepiped. Our application differs from that described by Dasgupta et al. in two details: the use of time-course development data and the type of kinetic model used to describe the respective data sets. The discussion by Dasgupta et al. indicates that they had envisioned application of the method to data obtained at a single value of Xt, since they performed a sensitivity analysis to identify the best Xt. However, the optimum is also a function of the mass transfer coefficient, h, so if the system being examined exhibits a wide range of coefficients, a Xt that works well for one part of the range may yield results that are insensitive to h at another part of the range. Therefore we collected OD data for a range of times from 2–64 min and fit the calibration curve to the entire time course at each location. The range of time assures that a broad range of coefficient values can be determined with good sensitivity. From Table 1 it can be seen that mass transfer coefficients spanning close to an order of magnitude were obtained, while the standard error for the coefficients, expressed as a fraction of the central estimate, is 1.3±0.4% (mean±s.d. for the 14 estimates).

As mentioned by Dasgupta et al. [1], the diffusing species may not be hydroquinone since a number of other developing agents are present in commercial developers. However, the behavior of equations (11) and (12) depends only on the ratio, β'/h. Suppose that the actual diffusivity of the developing agent is $D_H^* = f\cdot(8.3\cdot10^{-10}\ \mathrm{m^2\ s^{-1}})$ for some $f > 0$, and that, using $f = 1$ in performing our calibration, we obtained an estimate of β' equal to β'_0. Then the actual value of β'

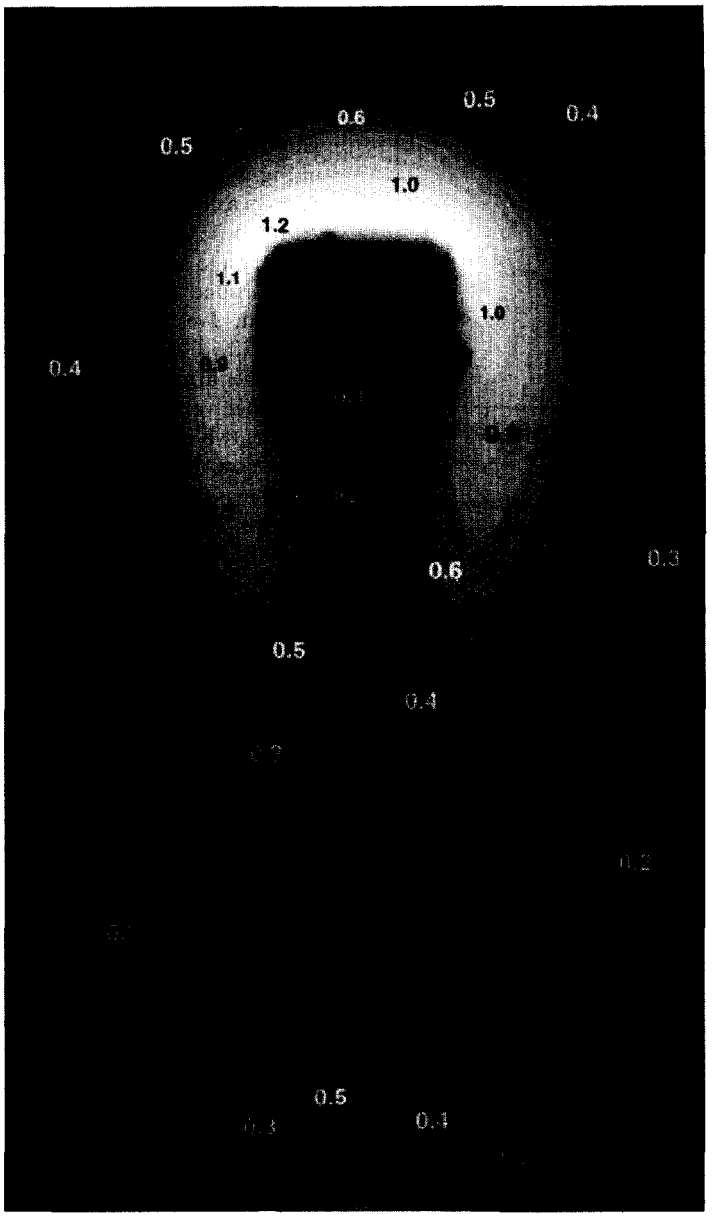

Fig. 8. Map of mass transfer coefficients from the flow tank floor in the region around the parallelepiped (PPD). The dark, square area in the top center is the PPD footprint. The numbers are values of the coefficients (10^{-5} m s^{-1}) at the contour lines.

would be $\beta'^{*} = f^{2/3} \cdot \beta'_0$, since substitution of both β'^{*} and D_H^* in place of β'_0 and D_H would yield identical predictions for the relationship between Xt and OD in the equations above. Further, if we obtained a value of $h = h_0$ after application of the calibration equation using $\beta = \beta'_0$, then actual value of h in the flow tank would be $h^* = f^{2/3} \cdot h_0$. However, for transport in dilute solutions in a number of geometries, including flow over a flat plate, the Chilton–Colbourn j-factor correlation gives proportionality between h and $D_H^{2/3}$ [14], so this dependence should also hold for h values in the flow tank. If so, then the predicted mass transfer coefficient will be $h_0 = h^*/f^{2/3}$; i.e., the mass transfer coefficient for a compound with diffusivity equal to $8.3 \cdot 10^{-10}$ m^2 s^{-1}. Therefore we can still expect good agreement between CFD predictions and the experimentally determined mass transfer coefficients (provided that the same value of D_H is used in both), even though the absolute values for both may be in error relative to that of the actual developing agent.

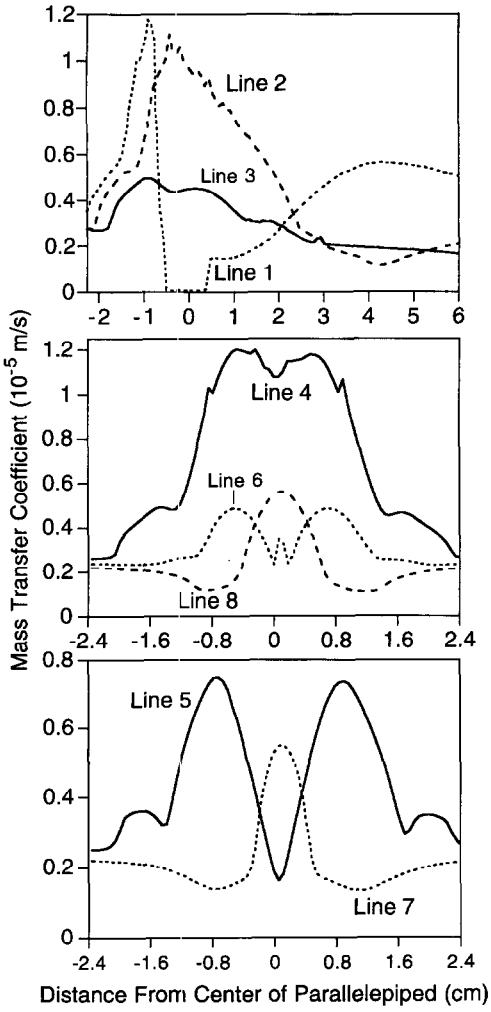

Fig. 9. Values of the mass transfer coefficient along lines indicated in Fig. 4(B).

There are two possible explanations for the difference in model choice between noncatalytic and autocatalytic forms: the difference in film, developer, or both, and the range of Xt over which data were collected. The difference in the fits of the two models to the data of Dasgupta et al. [1] was less obvious than we observed. Differences in quantitative goodness of fit were small in both cases, but they favored the noncatalytic model. Also, the value they obtained for C_{SB0}/C_{S0} for the autocatalytic was deemed unrealistically small. The difference between their results and ours could be due to the difference in film and developer used, or because we obtained OD measurements at very low Xt values that better showed the sigmoidal character of the development curve. The first possibility would require further experimental investigation, which is not directly germane to our goal. The second arises from the clustering of our data at fairly short Xt values, while Dasgupta et al. used a much more uniform design. They might have selected the autocatalytic model if a different experimental design had been used. Still, In Fig. 6, dropping the short Xt values from our data would probably not alter our conclusion, since the inflection point occurs about half-way through the development process ($\sim$3.2 min·%). The time course reported by Dasgupta et al. is only consistent with an inflection point occurring no later than 1/3 of the way through development, and any upward concavity early in their data is very slight. The concavity in our data, though slight, appears quite real. This suggests that the difference in film and developer is the causative factor.

A possible source of error is the use of Xt values up to $\sim$22 min·% in the flow tank experiments, while a maximum of 6.4 min·% was used in the SD experiments. Greater values of Xt were not used in the SD experiments because, over the range of rotational speeds used, ODs over 4.0 occurred for Xt much greater than 6.4 min·%. At lower rotational speeds, greater Xt values would be needed to obtain optical saturation, but the rotator could not be operated reliably at lower speeds—the rotation became jerky and the film disk would fall off. By using flow tank data obtained at higher Xt values, we are extrapolating to lower mass transfer coefficients (i.e., between 0 and that which occurs from 40 rpm). Since one would observe zero development at $Xt = 0$, it could be argued that, while extrapolating in Xt, we are interpolating mass transfer coefficients. Therefore we felt that the use of data for $Xt > 6.4$ min·% was not inappropriate. Given that the model described the entire range of data in Fig. 7 fairly well, we decided to use the entire range of Xt values from the flow tank, rather than restricting Xt to $\leqslant$6.4 min·%. But this extrapolation may explain the lack of fit for the lowest curve in Fig. 7 at low Xt values as compared to high Xt.

The lack of fit for the lowest curve in Fig. 7 could also be due to differences in the way that the film was handled in the SD experiments as compared with the flow tank experiments. In the SD experiments, the film was dipped in water prior to placement on the disk surface, allowing the emulsion to begin swelling before it came into contact with developer, but then there was minimal time between immersion of the disk in the developer solution and starting of the rotator. In contrast, the film was not dipped in water before placement into the flow tank and, more importantly, some time was required to place the sheet of film on the flow tank floor and then position the PPD. Experimental time for the flow tank was measured from the moment when the PPD was placed on the film, not from the moment of first immersion. Since the delay in placing the film and PPD in the flow tank would disproportionately affect the short Xt data, correcting for it would tend to shift those data downward or to the left, leading to a better fit. In fact, the decision to include the long Xt data followed in part from the realization that

this uncounted time was a much smaller fraction of the total time for those experiments.

6. Conclusions

A previously developed photographic method for quantifying mass transfer from an aqueous solution to a wall can be applied to an alternate film and developer combination (Kodak Technical Pan Film, TP4415, 8 in × 10 in, Estar Thick Base; Kodak HC-110 developer). This film/developer combination yielded sharper contrast between areas of high and low uptake compared to other film types. Moreover, the method can be applied to time-course data, allowing one to assure maximal sensitivity in the parameter estimation process without a priori knowledge of mass transfer resistance in the system of interest. As opposed to the apparently noncatalytic kinetics observed by Dasgupta et al. [1] for Kodak Plus-X film and D-76 developer, our results indicate autocatalytic kinetics, where reduced silver (a small amount of which exists in the latent image after light exposure) is presumed to act as a catalyst for the reduction process. Finally, an automated parameter estimation process was devised to apply the calibration method to very large data sets to generate a detailed map of mass transfer resistance over entire regions of a flat surface.

Acknowledgements

Primary thanks go to Dr James Ultman, Department of Chemical Engineering, Pennsylvania State University, University Park, PA, for the concepts underpinning this work as well as for his helpful suggestions and comments on the conduct of the research and in manuscript preparation. Dr Julie Kimbell and Dr Kevin Morgan at CIIT provided oversight and direction for the research. The authors thank Mr Donald Joyner at CIIT for his invaluable assistance with the flow tank experiments and Dr Peter Fedkiw, Department of Chemical Engineering, North Carolina State University, for the use of space in his laboratory and his RPM rotator for the spinning disk experiments as well as guidance in the design of the disk-spindle. We thank Dr Derek Janszen at CIIT for his assistance with the statistical analysis and Dr Bahman Asgharian at CIIT for his helpful comments during manuscript preparation.

References

[1] Dasgupta A, Guenard P, Anderson SM, Karsnitz JS, Ultman JS. Calibration of a photographic method for imaging mass transfer in aqueous solutions. Int J Heat Mass Transfer 1985;38:2029–37.

[2] Morgan KT, Kimbell JS, Monticello TM, Patra AL, Fleishman A. Studies of inspiratory airflow patterns in the nasal passages of the F344 rat and rhesus monkey using nasal molds: relevance for formaldehyde toxicity. Toxicol Appl Pharmacol 1991;110:223–40.

[3] Kimbell JS, Gross EA, Joyner DJ, Godo MN, Morgan KT. Application of computational fluid dynamics for regional dosimetry of inhaled chemicals in the upper respiratory tract of the rat. Toxicol Appl Pharmacol 1993;121:253–63.

[4] Keyhani K, Scherer PW, Mozell MM. Numerical simulation of airflow in the human nasal cavity. J Biomech Eng 1995;117:429–41.

[5] Lugt HJ. Vortex Flow in Nature and Technology. New York: John Wiley and Sons, 1983.

[6] Baker CJ. The laminar horseshoe vortex. J Fluid Mech 1978;95:347–67.

[7] Hunt JCR, Abell CJ, Peterka JA and Woo H. Kinematic studies of the flows around free or surface mounted obstacles; applying topology to flow visualization. J Fluid Mech 1978;86:179–200.

[8] Deng GB, Piquet J. Navier–Stokes computations of horseshoe vortex flows. Int J Numer Meth Fluids 1992;15:99–124.

[9] Goldstein RJ, Chyu MK, Hain RC. Measurement of local mass transfer on a surface in the region of the base of a protruding cylinder with a computer controlled data acquisition system. Int J Heat Mass Transfer 1985;28:977–85.

[10] Ichimiya K, Akino N, Kunugi T, Mitsushiro K. Fundamental study of heat transfer and flow situation around a spacer (in the case of a cylindrical rod as a spacer). Int J Heat Mass Transfer 1988;31:2215–25.

[11] Dasgupta A, Guenard P, Ultman JS, Kimbell JS, Morgan KT. A photographic method for the visualization of mass uptake patterns in aqueous systems. Int J Heat Mass Transfer 1993;36:453–62.

[12] Riddiford AC. The rotating disk system. Advances in Electrochemistry and Electrochemical Engineering 1966;4:47–116.

[13] Levich VG. Physicochemical Hydrodynamics. Englewood Cliffs, NJ: Prentice-Hall, 1962. pp. 60–9.

[14] Bird RB, Stewart WE, Lightfoot EN. Transport Phenomena. New York: John Wiley and Sons, 1960. pp. 642–8.

[15] McCabe WL, Smith JC, Harriot P. Unit Operations of Chemical Engineering, 4th ed. New York: McGraw-Hill, 1985, pp. 300–1.